



OPEN Polarization-independent dual-band quasi-bound states in the continuum based on graphene metasurface for tunable THz sensing application

Liyu Zhang^{1,2}, Hanxin Shen^{1,2} & Zhong Huang¹✉

To catch high quality (Q) factors is always pursued for optical resonators. In this study, polarization-independent dual-band quasi-bound states in the continuum (quasi-BIC) in a graphene-based metasurface is proposed for the first time in the terahertz regime. The quasi-BIC resonance modes with a Q factor of 176 is achieved by introducing symmetry breaking into the unit structure. The proposed metasurface is well analyzed, and both the numerical calculations and the coupled mode theory shows the Q-factors of dual quasi-BICs follow the inverse square dependence on the asymmetric parameter. To better understand the excitation mechanism of the quasi-BICs, we investigate the electric field distribution and surface current distribution. Notably, the quasi-BIC transmission spectra can be tuned up to 2.3 THz by varying the graphene's chemical potential, while keeping the modulation depth of the transmission larger than 50%. For the application, we further demonstrate biosensors with maximum sensitivity of 6.75 THz/RIU and minimum of the limit of detection of 0.0214 RIU. Unlike polarization-sensitive graphene quasi-BIC biosensors limited by complex alignment correction process with the light source, our proposed metasurface can maintain good quasi-BIC characteristics for arbitrarily polarized incident light and various angles of incidences ranging from 0 to 65°, which will greatly enhance the robustness of biosensors to rival the refractive index detection capabilities.

The ability to catch high quality (Q) factors is always desired for optical resonators when enhancing the light-matter interaction during the process of electromagnetic radiation^{1–3}. In recent decades, with the development of nanofabrication techniques, high Q optical resonators have triggered anomalous specific physical phenomena and have exceptional applications in lasers^{4,5}, filters^{6,7}, giant nonlinear enhancement^{8,9} and robustly perfect absorption⁷. Bound state in the continuum (BIC)^{10,11} is non-radiating eigenstates within a continuum spectrum with ultra-high Q factors. Ideally, an optical BIC has an infinite Q factor and zero linewidth, thus the BIC is concealed in the radiation continuum and cannot be detected. However, with inevitable material loss, roughness or fabrication imperfections, the BIC can be observed in a way of finite narrow bandwidth and high Q factor with finiteness (i.e., quasi-BIC). A quasi-BIC can also be artificially transformed from an ideal BIC in two ways: the symmetry-protected BIC (breaking the in-plane or the out-of-plane symmetry)¹² and the accidental BIC (tuning the parameter of the target system)¹⁰. Inspired by this novel and practical physical mechanism, various quasi-BIC metasurfaces have been intensively studied, especially in sensing applications. For example, Romano et al.¹³ achieved quasi-BICs which can detect liquids with different refractive indices in the visible light region. Li et al.¹⁴ designed silicon quasi-BIC metasurface achieving high refractive index sensitivities. Yin et al.¹⁵ fabricated quasi-BIC absorber with the structure of metal-insulator-metal (MIM) for sensing in the terahertz (THz) region. Nevertheless, most of quasi-BIC devices based on dielectric or metallic resonators can only work under a certain frequency once after the fabrication, which severely restricts the demand for flexible applications.

Recently, the dynamic tuning of the working frequency of quasi-BICs has attracted strong interests with optically active materials. By using photosensitive chalcogenide glass, Mikheeva et al.¹⁶ studied the tunable properties of quasi-BIC in both theory and experiment. Chen et al.¹⁷ fabricated a tunable terahertz quasi-BIC metasurface through controlling the temperature of strontium titanate materials. Liu et al.¹⁸, He et al.¹⁹ and Hou et al.²⁰ tuned the resonance frequency of quasi-BICs based on metasurface which supported by the 3D Dirac

¹School of Physics & Electronic Information, Jiangsu Second Normal University, Nanjing 210013, China. ²Liyu Zhang and Hanxin Shen contributed equally to this work. ✉email: huangzhong89@126.com

semimetals. Danaeifar²¹ and Roy et al.²² proposed a two-dimensional quasi-BIC metasurface for THz sensing based on graphene dimer resonators. Among the optically active materials, graphene has emerged as remarkable 2D material for tunable devices due to its high electron mobility, wide frequency response range, cost-effective and large area synthesis. More importantly, the electrical conductivity of the graphene can be stably controlled by the voltage or chemical doping²³. Although the thickness of the graphene is a single layer of carbon atoms, the light-matter interaction of the graphene can be strongly enhanced by the surface plasmon resonance in the THz region while keeping low ohmic loss²⁴. Thus, to incorporate graphene into the quasi-BICs will not only expand the scope of dynamically tunable BICs, but also will promote the development of high Q feasible 2D planar light-matter interactions. However, so far all the above-mentioned active quasi-BIC studies focus on anisotropic structures. The quasi-BICs obtained by breaking the symmetry can only be excited in a specific polarization direction. Overcoming the polarization limitation in the process of designing dynamically tunable BIC is needed far more in practice.

In this research, to the best of our knowledge, we propose polarization-independent dual quasi-BICs in a graphene-based metasurface for the first time. So far, all the above-mentioned tunable quasi-BICs focus on anisotropic structures, and they are polarization-sensitive. Compared to the polarization-sensitive quasi-BICs, the polarization-insensitive ones are more convenient for practical sensing applications because they can endure changes in polarization states of the incident waves, which eliminates the need for careful and precise alignment with the polarization direction of the laser source. Besides that, the dual band quasi-BICs can solve the time delay problem caused by the single band quasi-BIC when detecting a variety of gas and chemical solvents in sensing applications. After the optimization, dual graphene quasi-BIC resonances can be excited under normal incidence in THz region without breaking the C_{4v} symmetry. Compare with only one operating band, dual bands will reduce time delay introduced by modulation, especially in sensing applications in detecting a variety of gas and chemical solvents. Both the numerical calculations and the coupled mode theory (CMT) shows the Q-factors of dual quasi-BICs follow the inverse square dependence on the asymmetric parameter. The steady-state electric field distribution and surface current distribution further confirm that the metasurface can achieve dual-frequency quasi-BIC modes. Notably, the quasi-BIC spectra can be tuned up to 2.3 THz by varying the graphene's chemical potential, while keeping the modulation depth of the transmission larger than 50%. Based on the novel properties mentioned above, for the application, we demonstrate biosensors with maximum sensitivity of 6.75 THz/RIU and minimum LOD (the limit of detection) of 0.0214 RIU, which is superior to other types of THz sensors. Moreover, our proposed metasurface can maintain good quasi-BIC characteristics for arbitrarily polarized incident light and various angles of incidences ranging from 0 to 65°, which will greatly enhance the robustness of biosensors. We believe our work provides a valuable reference for actively tunable sensing devices and optical modulators with polarisation-independent, and will promote the development of the class of graphene quasi-BIC metasurfaces.

Structure design and methods

The schematic illustration of the structural super cell for the proposed dual-band polarization-independent graphene quasi-BIC metasurface is shown in Fig. 1a. The metasurface simply consists of a monolayer graphene film on the top of the SiO_2 substrate. The graphene film is patterned into a periodic array of coaxial apertures²⁵. Within the period of the unit cell, four coaxial apertures with a finite spacing are placed, as shown in Fig. 1b. The

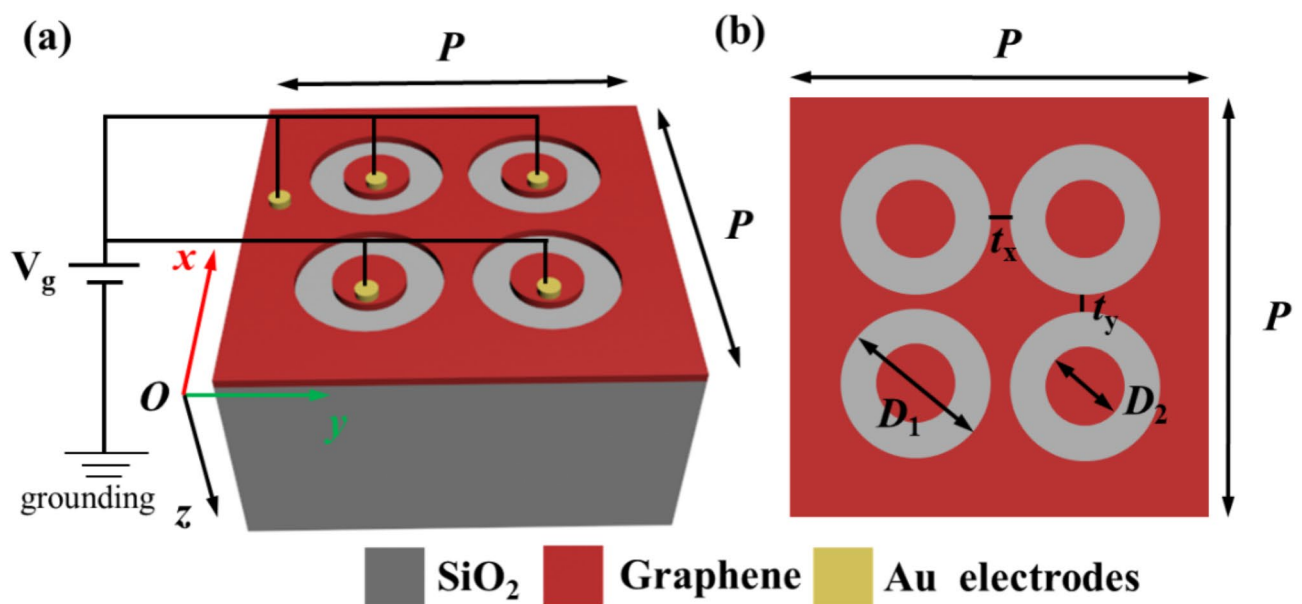


Fig. 1. (a) Schematic of the super cell for the proposed dual-band polarization-independent graphene quasi-BIC metasurface. (b) Unit cell of the proposed metasurface (vertical view).

thickness of silicon layer is semi-infinite along the positive direction of the z -axis. After the optimization, the outer and inner diameter of the graphene coaxial apertures D_1 and D_2 are 1.6 μm and 0.8 μm , respectively. The period $P_x = P_y = P$ is 4.8 μm . The gap distances between graphene coaxial apertures in a super cell are t_x and t_y in the x and y directions, respectively. The relative permittivity of the semi-infinite SiO_2 substrate is assumed to be 3.9²⁶. The surface conductivity of graphene σ_g is modeled with Kubo's formula²⁷, which is given by:

$$\sigma_g = \sigma_{\text{intra}} + \sigma_{\text{inter}}. \quad (1)$$

At far infrared THz frequencies, the interband component of the surface conductivity of graphene becomes negligible, so we have $\sigma_g \approx \sigma_{\text{intra}}$. The dominating intraband one could be approximated by a Drude model:

$$\sigma_g = i \frac{e^2 E_f}{\pi \hbar (\hbar \omega + i\tau)}, \quad (2)$$

where the reduced Planck's constant $\hbar = 1.0547 \times 10^{-34}$ J·s. The electron charge is $e = 1.602 \times 10^{-19}$ C. The chemical potential of the graphene is $E_f = 0.8$ eV, unless otherwise specified. The relaxation time of graphene is assumed to be 2 ps²², and ω is the angular frequency of the incident plane wave. When doing the full-wave simulation using the open source software 'East FDTD' based on finite difference time domain method^{28,29}, the thickness of the graphene layer is set to be $t = 0.34$ nm. The bulk complex dielectric constant of graphene can be calculated by the equation $\epsilon_g = 1 + i\sigma_g / (\epsilon_0 \omega t_g)$, and ϵ_0 is the permittivity in vacuum. $\omega = 2\pi f$ is the angular operating frequency. In the simulation process, we used transition boundary conditions to simulate graphene layer. Periodic boundary conditions are utilized in the x and y directions of the supercell, and perfectly matched layers are applied to the z direction under and above the supercell. For meshing the substrate, we choose a physics-defined mesh with finer settings. For the graphene boundary layer, a finer settings boundary mesh is defined, and the rest of the other regions with normal triangular elements mesh. For meshing the PML layers, we choose a square-mapped meshing with at least 10 divisions. For the fabrication of our proposed graphene quasi-BIC metasurface, one can follow the standard process³⁰ as below. First, the monolayer graphene film can be grown via chemical vapor deposition method in a high temperature tubular quartz tube with reaction gas mixtures (CH_4 , H_2 and Ar) on a thick Ni or Cu film. Then, the polymer supports such as soft poly(dim-ethylsiloxane) (PDMS) stamps and thermal-release tapes are attached to the graphene films grown on metal layers. The support/graphene/metal layers are soaked with FeCl_3 solution to remove metal layers, and then the resulting graphene film on the polymer support is ready to be transferred onto the SiO_2 substrates. After removing the polymer supports, focused ion beam milling (FIBM) is employed to pattern the graphene films into a periodic array of coaxial apertures. Finally, Au nano-electrodes array and grounding are patterned on top of graphene to form contacts to modulate the chemical potential of graphene by controlling the changes of carrier concentration.

Results and discussion

Figure 2a depict the transmission spectra contour of the graphene quasi-BIC metasurface impinged by x -polarized THz wave at normal incidence under perturbation. When the gap distances $t_x = t_y = t_0 = 800$ nm, we label the metasurface as original state and no perturbation happens. For the perturbation, four graphene coaxial apertures are moved toward the center of the supercell synchronously in both x and y directions, as shown in Fig. 1, and the gap distances t_x and t_y change simultaneously. Here we define the gap distance offset $\Delta t = t_0 - t_x$ (t_y). For example, when $t_x = t_y = 700$ nm, the gap distance offset $\Delta t = 800 - 700 = 100$ nm. From Fig. 2a, it can be seen that we move towards the higher or lower values of the Δt , two transmission dips become prominent, and the resonant dips gradually becomes broad. The frequency of two transmission dips also redshifts. When $\Delta t = 0$, two transmission dips have zero bandwidth, which cannot be inspected from the transmission spectrum, indicating the existence of two BIC modes. The two BIC modes in Fig. 2a are labeled as BIC-I and BIC-II in the higher and lower frequency (red dash circles), respectively. To illustrate the evolution of the quasi-BIC transformed from BIC explicitly, a few particular transmission spectra are displayed in Fig. 2b. When $\Delta t = 200$ nm, the first quasi-BIC mode named as Q-BIC-I start to appear in the transmission spectra, while the second quasi-BIC mode named as Q-BIC-II creeps in until $\Delta t = 400$ nm. In Fig. 2c the Q factors of the dual quasi-BIC modes are plotted with different asymmetric parameter α . α is defined as $\alpha = \Delta t/t_0$, and the Q factor is defined as³¹:

$$Q = \frac{f_{\text{dip}}}{\gamma}, \quad (3)$$

where f_{dip} is the transmission dip frequency, and γ is the corresponding full-width at half maximum (FWHM). It can be seen that the Q factor of both dual quasi-BIC modes gradually increases as the asymmetric parameter α decreases. At $\alpha = 0.875$, the Q factors of mode Q-BIC-I and Q-BIC-II are 69 and 70, respectively. When α drops to 0.2, the Q factor of mode Q-BIC-I increases to 176. The dependence of Q-factor on α meet the law of $Q \propto \alpha^{-2}$.

The Q factors versus asymmetric parameters plotted in Fig. 2c are obtained by fitting the simulated results with a normalized Fano profile equation³²:

$$T = C_0 + \frac{[2(f - f_{\text{dip}})/\gamma + \beta]^2}{[4(f - f_{\text{dip}})^2/\gamma^2 + 1](1 + \beta^2)}, \quad (4)$$

where T represents the transmittance. C_0 represents the Fano fitting constant. f represents the frequency of normal incident plane wave. β represents the Fano parameter. The Fano fitting results and numerical calculated

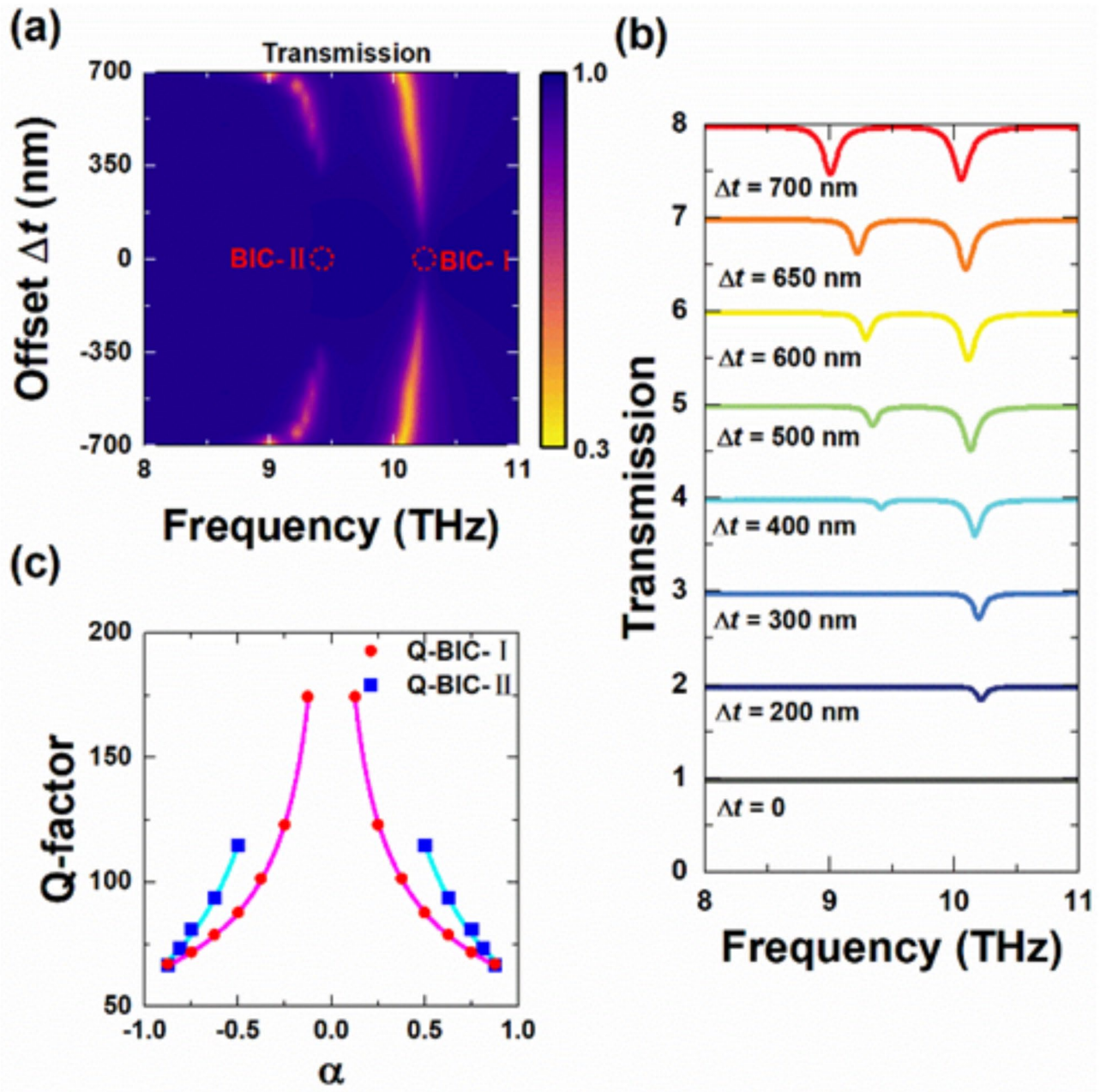


Fig. 2. (a) Transmission contour of the graphene quasi-BIC metasurface. (b) Evolution of the transmission spectra with various gap distance offset Δt . (c) Q-factors of dual quasi-BIC modes versus asymmetric parameter.

transmission are agreed well in Fig. 3b, with $C_0 = 0.97$, $\beta = 0.018$, $\gamma = 0.147$ THz for mode Q-BIC-I, and $\gamma = 0.129$ THz for mode Q-BIC-II. In order to derive and analyze the underlying physical mechanism of the quasi-BIC resonances, the coupled mode theory (CMT)³³ is performed and compared with the simulated transmission spectrum in Fig. 3a as following:

$$\begin{bmatrix} f - f_1 - i\gamma_1 & \Omega_{12} & \Omega_{13} & \Omega_{14} \\ \Omega_{21} & f - f_2 - i\gamma_2 & \Omega_{23} & \Omega_{24} \\ \Omega_{31} & \Omega_{32} & f - f_3 - i\gamma_3 & \Omega_{34} \\ \Omega_{41} & \Omega_{42} & \Omega_{43} & f - f_4 - i\gamma_4 \end{bmatrix} \begin{bmatrix} a \\ b \\ c \\ d \end{bmatrix} = \begin{bmatrix} \sqrt{\gamma_1} E \\ \sqrt{\gamma_2} e^{i\phi_1} E \\ \sqrt{\gamma_3} e^{i\phi_2} E \\ \sqrt{\gamma_4} e^{i\phi_3} E \end{bmatrix}, \quad (5)$$

where the resonance frequency of the for resonators in a super cell is represented by $f_{1(2,3,4)}$, and the corresponding FWHM is represented by $\gamma_{1(2,3,4)}$. Ω_{ij} ($i, j = 1, 2, 3, 4$) is the coupling coefficient. a, b, c and d are the complex amplitudes of different resonance modes. E is the complex amplitude of the incident THz wave. $\phi_{1(2,3)}$ is the

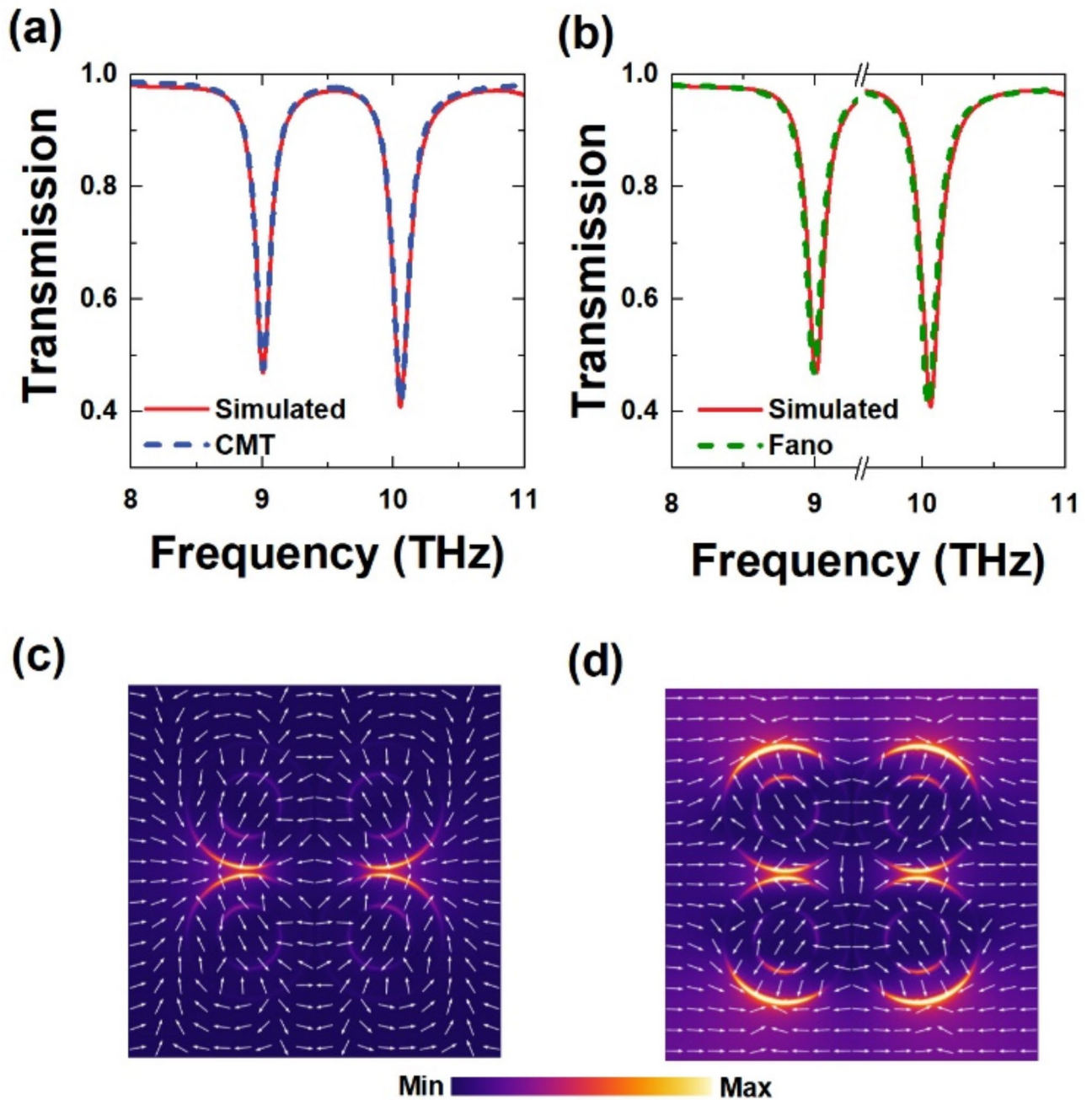


Fig. 3. (a) CMT and (b) Fano-fitting of the quasi-BIC transmission spectra (red solid line) at $\Delta t = 700$ nm. Top view of $|E|$ field distribution (color) and surface current distribution (white arrows) on the x - y plane at (c) 9.04 THz and (d) 10.12 THz.

phase information. Since only two resonance modes appear in the transmission spectrum, the four resonance frequencies ($f_{1(2,3,4)}$) degenerate into two resonance frequencies ($f_{1(2)}$). The CMT is simplified as:

$$\begin{aligned} a(f - f_1 - i\gamma_1) + b\Omega_{12} &= \sqrt{\gamma_1}E \\ a\Omega_{21} + b(f - f_2 - i\gamma_2) &= \sqrt{\gamma_2}e^{i\phi}E, \end{aligned} \quad (6)$$

with $\Omega_{12} = \Omega_{21} = g - i\sqrt{\gamma_1\gamma_2}e^{i\phi}$, where g represents the coupling strength and can be obtained as the fitting parameter. The entire transmission spectrum is then given by:

$$T = 1 - \text{imag} \left(\frac{\gamma_2(f - f_1 - i\gamma_1)e^{2i\phi} + \gamma_1(f - f_2 - i\gamma_2) - 2g\sqrt{\gamma_1\gamma_2}e^{i\phi}}{(f - f_1 - i\gamma_1)(f - f_2 - i\gamma_2) - g^2} \right), \quad (7)$$

and the match with the numerical spectra is shown in Fig. 3a with $g=0.89$ and $\phi=1.76$. The results analyzing by CMT are in good agreements with that by numerical simulation.

To better understand the excitation mechanism of the quasi-BIC and electromagnetic waves transfer energy, the mode profiles of the Q-BIC-I dip and the Q-BIC-II dip are shown in Fig. 3d,c, respectively. The $|E|$ profile in the x - y plane calculated on the graphene layer in Fig. 3c indicates that the electric-field intensity is localized between the edges of coaxial apertures along the illuminated polarization for the plasmonic mode Q-BIC-II. More interestingly, at the resonant frequency of plasmonic mode Q-BIC-I, the electric-field intensity is not only localized between the edges of coaxial apertures inside the super cell, but also with a more concentration of hotspots between the adjacent super cells along the illuminated polarization, as shown in Fig. 3d. To further investigate the origin of the resonance, the surface current distributions are also plotted. Both the surface current distributions in Fig. 3c,d show the trend of accumulation of electrons, which generates strong energy confinement and narrow local hotspots, which is important for the application in the areas of sensing. Both the steady-state electric field distribution and surface current distribution confirm that the metasurface can achieve dual-frequency quasi-BIC modes.

The most attractive feature of graphene is its surface conductivity which can be tuned by thermal stimulation, and electrical or chemical doping³⁴. In Fig. 4a, we discuss the active modulation of the quasi-BIC by tuning the chemical potential. For our structure ($\alpha=0.875$), the chemical potential of the graphene can be dynamic reconfigured by applying a gate bias voltage^{35,36}, as shown in Fig. 1. It can be seen that as the chemical potential increases, the overall quasi-BIC transmission dips shift towards higher frequencies. This is because the intraband conductivity of the graphene changes with the increasing of the chemical potential, and make the graphene behaves more like semi-metallic, resulting in a blueshift in the resonant frequency. Besides the frequency shift, we also define an amplitude modulation to quantify the modulation depth of the transmission as following:

$$\Delta T_{max} = (T_{max} - T_{min}) \times 100\%, \quad (8)$$

where T_{max} and T_{min} are the maximum and minimum values of transmittance. Figure 4a shows that ΔT_{max} gradually increases with the increasing of chemical potential. At $E_f=0.70$ eV, the modulation depth $\Delta T_{max}=50\%$. At $E_f=0.90$ eV, the modulation depth increases to $\Delta T_{max}=62\%$.

Compared to the polarization-dependent quasi-BICs, polarization-independent ones are more desired for practical use because they are immune to the changes of polarization states and angle. However, all dynamic tuning quasi-BICs presented thus far^{16–22} are highly sensitive to the polarization angle of incident waves, and can be only supported for a predefined linear polarization state. It is somehow because the symmetry-protected quasi-BICs are easier to be realized by breaking the in-plane symmetry³⁷. The polarization-independent characteristics of our graphene quasi-BIC metasurface are investigated in Fig. 4b. Here we choose $E_f=0.85$ eV, while keeping other geometric parameters unchanged ($\alpha=0.875$). It can be seen that the quasi-BIC-I transmission dip is constantly maintained at 10.44 THz for all polarization directions on the x - y plane, with ΔT_{max} larger than 60%. Similar to the quasi-BIC-I, the quasi-BIC-II transmission dip is constantly maintained at 9.31 THz with ΔT_{max} larger than 50%. This is because when the asymmetric parameter α is introduced, we keep the gap distances $t_x=t_y$ in the x and y directions, which meet the requirement of C_{4v} symmetry in the square super cell³⁸. Polarization-independent quasi-BIC devices are convenient for practical use, especially in sensing application. It can reduce complex alignment processes, and make the device work under arbitrarily polarized incident light.

The sensing performance of the proposed graphene quasi-BIC metasurface is then studied in Fig. 5. Here the asymmetric parameter is $\alpha=0.875$. When increasing the refractive index of the surrounding medium from 1.00

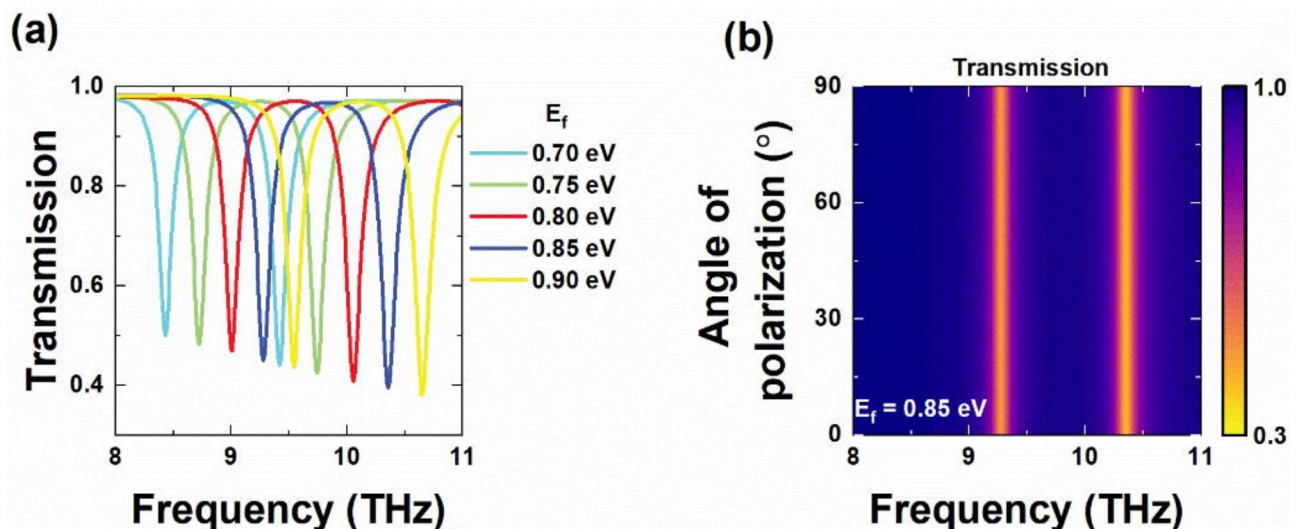


Fig. 4. (a) Transmission spectra with E_f ranging from 0.70 eV to 0.90 eV while keeping $\alpha=0.875$. (b) Transmission contour as a function of polarization angle and incident THz wave frequency.

to 1.04, the dual quasi-BIC transmission dips basically do not change, but shift toward lower frequency, as can be seen in Fig. 5a,c, which is promising for liquid and gas sensing. In order to evaluate the quality of a sensor, the sensitivity is defined as $S = \Delta f / \Delta n$, where Δf represents the frequency difference between two adjacent refractive indices, with $\Delta n = 0.01$. The calculated sensitivity of mode quasi-BIC-I is shown in Fig. 5b. The frequency shifts corresponding to different refractive indexes exhibit a linear dependence with a slope of 6.75 THz/RIU, ensuring that even a slight change in the refractive index of the surrounding medium can be detected by our proposed metasurface through the measurement of the redshift of the transmission spectra. The calculated sensitivity of mode quasi-BIC-II is 6.02 THz/RIU, and the frequency shifts corresponding to different refractive indexes are shown in Fig. 5d. Besides the sensitivity, the sensing performance can also be quantified by the figure of

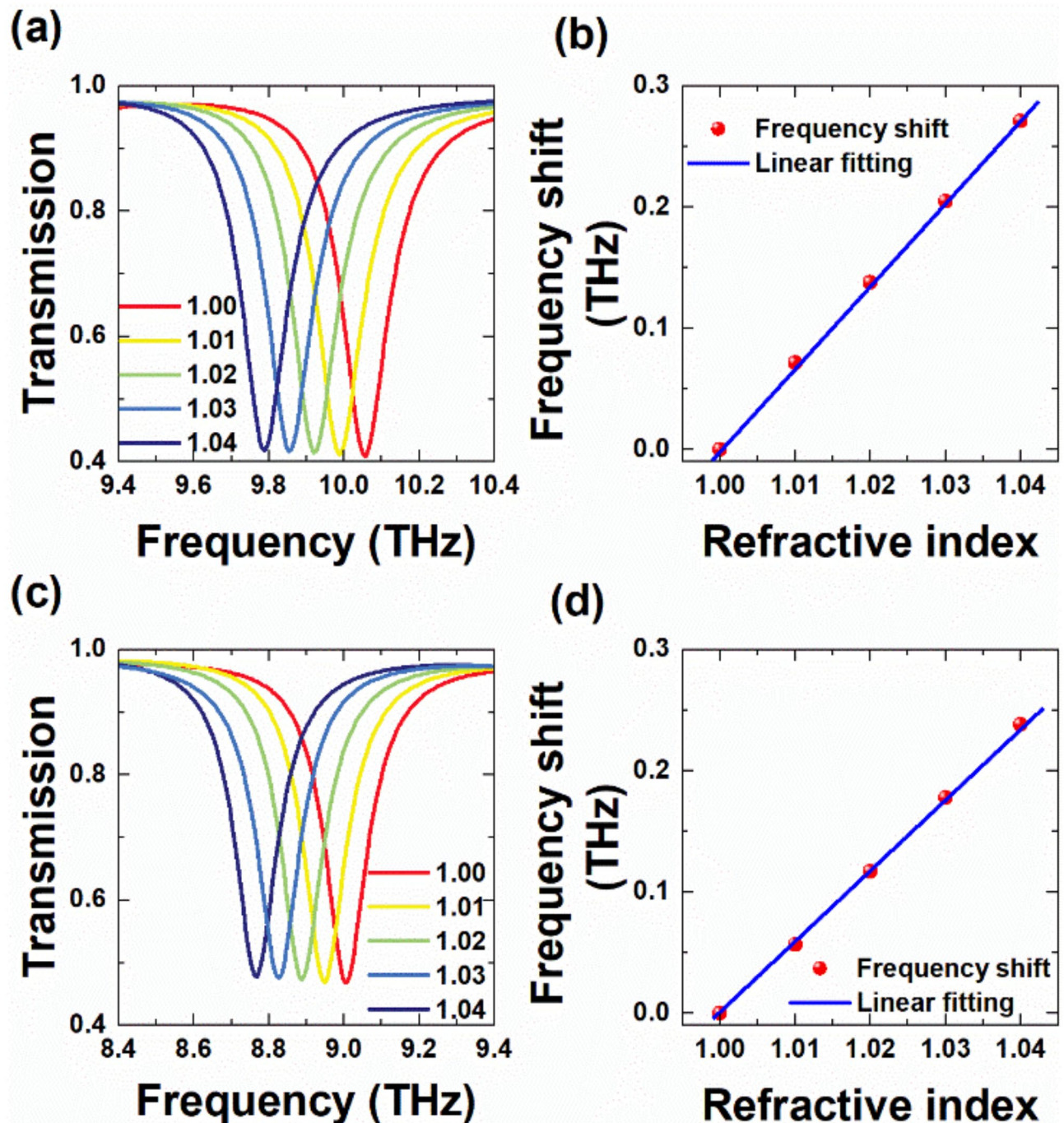


Fig. 5. (a) Transmission spectra with versus different refractive indices for mode quasi-BIC-I. (b) The relationship between frequency offset and refractive index for mode quasi-BIC-I. (c) Transmission spectra with versus different refractive indices for mode quasi-BIC-II. (d) The relationship between frequency offset and refractive index for mode quasi-BIC-II.

Ref	Sensitivity (THz/RIU)	FOM (RIU ⁻¹)	Q-factor	Tunability (Y: yes, N: no)	Polarization sensitivity (De: dependent, Inde: independent)
³⁹ (2019)	13.25	36.51	16.79	Y	De
⁴⁰ (2021)	2.26	189.9	706	N	De
⁴¹ (2015)	1.908	6.57	19.83	Y	Inde
⁴² (2015)	1.48	20.5	48.2	N	Inde
¹⁵ (2022)	0.187	28.58	235	N	De
⁴³ (2022)	0.266	40.65	162	N	De
This work	6.75	45.87	69	Y	Inde
	6.02	46.72	70	Y	Inde

Table 1. Comparison of sensing performance of the proposed graphene quasi-BIC metasurface.

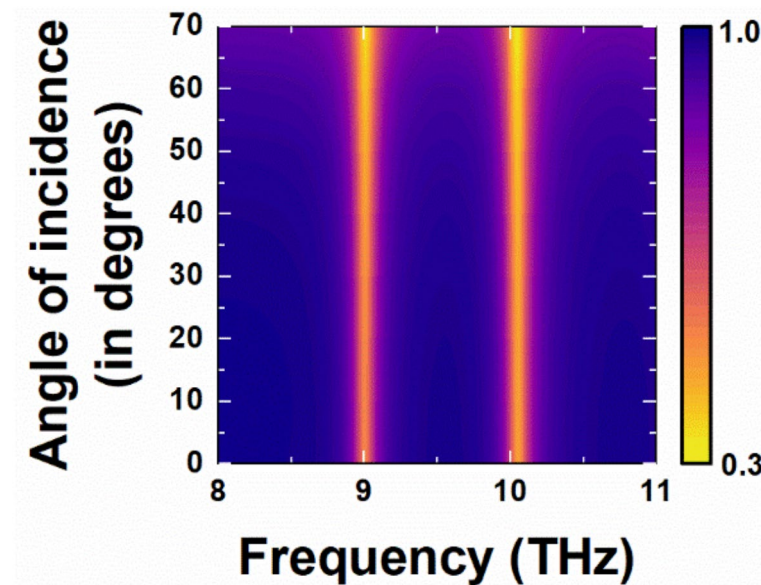


Fig. 6. Transmission contour related to the incident angle (in y - o - z plane).

merit (FOM), which is given by $FOM = S/\gamma$. The Q-factor plays a crucial role here, and a large FOM value is desirable for a particular sensor. The $LOD = 1/FOM$ of mode quasi-BIC-I and quasi-BIC-II are calculated to be 0.0218 RIU and 0.0214 RIU, respectively. To further rival the refractive index detection capabilities of our proposed graphene quasi-BIC metasurface, a comparison of THz sensor data information collected from recent literatures is presented in Table 1. We can see most of the THz sensors are lithography-based structures, which are passive, cost-ineffective and lack dynamicity at the operation's wavelength region. On the contrary, our surface conductivity-based structures are active that maintain the same lithographical configuration. Besides, our proposed polarization-independent graphene quasi-BIC metasurface offers improved performance over the previous works. Although the sensitivity of Ref.³⁹ is higher than that of our work, however, the structures suggested by Ref.⁴⁰ is polarization-dependent, which can be only supported for a predefined linear polarization state. Other parameters such as the Q-factors, the tunability, and polarization sensitivity are also listed in Table 1 for the comparison.

At the end of this paper, we discuss the angle-dependent property of our proposed graphene quasi-BIC metasurface ($\alpha = 0.875$). Figure 6 shows the transmission contour related to the incident angle (in y - o - z plane). The transmission spectrum maintains good quasi-BIC characteristics for various angles of incidences ranging of 0–65°. The FWHM of mode quasi-BIC-I and quasi-BIC-II overall maintain at 0.147 THz and 0.129 THz, respectively. The modulation depth of the two modes are both larger than 50%. At higher angles > 65°, the transmittance begins decreases with a slight shift in the spectrum. This is because when the period P of our proposed structure is much smaller than the wavelength of incident THz wave, the phase difference of the light field at neighboring graphene coaxial apertures is rather independent of the incident angle, which results in that the resonance frequencies are loosely dependent on the incidence angle.

Conclusion

In this study, we propose a novel polarization-independent graphene quasi-BIC metasurface with dual THz working bands. The two quasi-BICs are achieved by perturbation while keeping the requirement of C_{4v} symmetry in the square super cell. The finite value of Q-factor can be up to 176, and follows the asymmetry

parameter as, $Q \propto \alpha^{-2}$. To better understand the underlying physical mechanism of the dual quasi-BICs, the analytical study has been carried out by Fano-fitting and CMT along with the simulation results. The steady-state electric field distribution and surface current distribution also confirm that the metasurface can achieve dual-frequency quasi-BIC modes. It is significant that the quasi-BIC spectra can be tuned up to 2.3 THz by varying the graphene's chemical potential, while keeping the modulation depth of the transmission larger than 50%. For the application of our proposed metasurface, we demonstrate biosensors with maximum sensitivity of 6.75 THz/RIU and minimum LOD of 0.0214 RIU, which is superior to other types of THz sensors. Moreover, our proposed metasurface can maintain good quasi-BIC characteristics for arbitrarily polarized incident light and various angles of incidences ranging from 0 to 65°, which will greatly enhance the robustness of biosensors. We believe our work provides a valuable reference for actively tunable sensing devices and optical modulators with polarisation-independent, and will promote the development of the class of graphene quasi-BIC metasurfaces.

Data availability

The datasets used and/or analyzed during the current study are available from the corresponding author upon reasonable request.

Received: 12 August 2024; Accepted: 24 March 2025

Published online: 07 April 2025

References

- Han, Z. et al. Significantly enhanced second-harmonic generations with all-dielectric antenna array working in the quasi-bound states in the continuum and excited by linearly polarized plane waves. *Nanophotonics* **10**(3), 1189 (2021).
- Zhou, C. et al. Bound states in the continuum in asymmetric dielectric metasurfaces. *Laser Photonics Rev.* **17**(3), 2200564 (2023).
- Aigner, A. et al. Continuous spectral and coupling-strength encoding with dual-gradient metasurfaces. *Nat. Nanotechnol.* **19**, 1804 (2024).
- Kodigala, A. et al. Lasing action from photonic bound states in continuum. *Nature* **541**(7636), 196–199 (2017).
- Ha, S. T. et al. Directional lasing in resonant semiconductor nanoantenna arrays. *Nat. Nanotechnol.* **13**(11), 1042–1047 (2018).
- Vallejo, M. L., Ladrón de Guevara, M. L. & Orellana, P. A. Triple Rashba dots as a spin filter: Bound states in the continuum and Fano effect. *Phys. Lett. A* **374**(48), 4928–4932 (2010).
- Foley, J. M., Young, S. M. & Phillips, J. D. Symmetry-protected mode coupling near normal incidence for narrow-band transmission filtering in a dielectric grating. *Phys. Rev. B* **89**(16), 165111 (2014).
- Wang, T. & Zhang, X. Improved third-order nonlinear effect in graphene based on bound states in the continuum. *Photonics Res.* **5**(6), 629–639 (2017).
- Wang, T. & Zhang, S. Large enhancement of second harmonic generation from transition-metal dichalcogenide monolayer on grating near bound states in the continuum. *Opt. Express* **26**(1), 322–337 (2018).
- Hsu, C. W. et al. Bound states in the continuum. *Nat. Rev. Mater.* **1**(9), 1–13 (2016).
- Azzam, S. I. & Kildishev, A. V. Photonic bound states in the continuum: From basics to applications. *Adv. Opt. Mater.* **9**(1), 2001469 (2021).
- Ni, L. et al. Tunable optical bound states in the continuum beyond in-plane symmetry protection. *Phys. Rev. B* **94**(24), 245148 (2016).
- Romano, S. et al. Tuning the exponential sensitivity of a bound-state-in-continuum optical sensor. *Opt. Express* **27**(13), 18776–18786 (2019).
- Li, B. et al. Asymmetric excitations of toroidal dipole resonance and the magnetic dipole quasi-bound state in the continuum in an all-dielectric metasurface. *Opt. Mater. Express* **11**(7), 2359–2368 (2021).
- Yin, W. et al. THz absorbers with an ultrahigh Q-factor empowered by the quasi-bound states in the continuum for sensing application. *Opt. Express* **30**(18), 32162–32173 (2022).
- Mikheeva, E. et al. Photosensitive chalcogenide metasurfaces supporting bound states in the continuum. *Opt. Express* **27**(23), 33847–33853 (2019).
- Chen, Xu. & Fan, W. Tunable bound states in the continuum in all-dielectric terahertz metasurfaces. *Nanomaterials* **10**(4), 623 (2020).
- Liu, H. et al. Realization of tunable dual-type quasi-bound states in the continuum based on a Dirac semimetal metasurface. *Opt. Mater. Express* **12**(7), 2474–2485 (2022).
- He, X. et al. 3D Dirac semimetals supported tunable terahertz BIC metamaterials. *Nanophotonics* **11**(21), 4705–4714 (2022).
- Hou, B. et al. Enhanced quasi-BIC refractive index sensing based on controlling the Fermi energy of Dirac semimetal metasurface. *Opt. Laser Technol.* **164**, 109537 (2023).
- Danaeifar, M. Quasi-bound state in the continuum based strong light confinement in graphene metasurfaces. *Opt. Mater. Express* **14**(2), 319–327 (2024).
- Roy, S., Mondal, S. & Debnath, K. Symmetric bound states in the continuum in an all graphene metasurface—Design and sensor applications. *IEEE Sens. J.* **23**(8), 8352–8359 (2023).
- Avouris, P. & Freitag, M. Graphene photonics, plasmonics, and optoelectronics. *IEEE J. Sel. Top. Quantum Electron.* **20**(1), 72–83 (2013).
- Nikitin, A. Y. et al. Surface plasmon enhanced absorption and suppressed transmission in periodic arrays of graphene ribbons. *Phys. Rev. B—Condens. Matter Mater. Phys.* **85**(8), 081405 (2012).
- Shen, Z. et al. Terahertz plasmonic nanotrapping with graphene coaxial apertures. *Phys. Rev. A* **102**(5), 053507 (2020).
- Huang, Z. et al. Excitation of tunable dual quasi-bound states in the continuum in graphene metasurface and terahertz sensing application. *Plasmonics* **18**(6), 2285–2293 (2023).
- Amin, M., Farhat, M. & Bağcı, H. A dynamically reconfigurable Fano metamaterial through graphene tuning for switching and sensing applications. *Sci. Rep.* **3**(1), 2105 (2013).
- Tang, C. et al. Ultra-broadband near-infrared absorption enhancement of monolayer graphene by multiple-resonator approach. *Diamond Rel. Mater.* **141**, 110607 (2024).
- Wu, Y. et al. Bandwidth tunability of graphene absorption enhancement by hybridization of delocalized surface plasmon polaritons and localized magnetic plasmons. *Discov. Nano* **19**(1), 19 (2024).
- Cakmakyan, S. et al. Gold-patched graphene nano-strips for high-responsivity and ultrafast photodetection from the visible to infrared regime. *Light: Sci. Appl.* **7**(1), 20 (2018).
- Koshelev, K. et al. Asymmetric metasurfaces with high-Q resonances governed by bound states in the continuum. *Phys. Rev. Lett.* **121**(19), 193903 (2018).
- Niu, J. et al. Resonance-trapped bound states in the continuum in metallic THz metasurfaces. *Opt. Lett.* **46**(2), 162–165 (2021).

33. Huang, W. et al. Universal coupled theory for metamaterial bound states in the continuum. *New J. Phys.* **23**(9), 093017 (2021).
34. Guo, B. et al. Graphene doping: A review. *Insciences J.* **1**(2), 80–89 (2011).
35. Al Sayem, A. et al. Ultrathin ultra-broadband electro-absorption modulator based on few-layer graphene based anisotropic metamaterial. *Opt. Commun.* **384**, 50–58 (2017).
36. Rodrigo, D. et al. Mid-infrared plasmonic biosensing with graphene. *Science* **349**(6244), 165–168 (2015).
37. Xu, K., Huang, J. & Wang, W. Broadband perfect optical absorption enabled by quasi-bound states in the continuum in graphene non-concentric rings. *Phys. Chem. Chem. Phys.* **25**(1), 604–611 (2023).
38. Cai, Y. et al. Enhancing light absorption of graphene with dual quasi bound states in the continuum resonances. *J. Quant. Spectrosc. Radiat. Transf.* **283**, 108150 (2022).
39. Nejat, M. & Nozhat, N. Ultrasensitive THz refractive index sensor based on a controllable perfect MTM absorber. *IEEE Sens. J.* **19**(22), 10490–10497 (2019).
40. Kameshkov, O., Gerasimov, V. & Knyazev, B. Numerical optimization of refractive index sensors based on diffraction gratings with high aspect ratio in terahertz range. *Sensors* **22**(1), 172 (2021).
41. Zhang, Y. et al. A graphene based tunable terahertz sensor with double Fano resonances. *Nanoscale* **7**(29), 12682–12688 (2015).
42. Wang, B.-X. et al. A novel dual-band terahertz metamaterial absorber for a sensor application. *J. Appl. Phys.* **117**(1), (2015).
43. Cen, W. et al. Ultrasensitive flexible terahertz plasmonic metasurface sensor based on bound states in the continuum. *IEEE Sens. J.* **22**(13), 12838–12845 (2022).

Acknowledgements

This work was supported by National Natural Science Foundation of China (NSFC) under Grant No. 11904139.

Author contributions

Z.H. proposed the research topic and supervised the work. L.Z. performed the numerical modelling. H.S. analyzed the results. Both authors participated in the discussion and prepared the manuscript.

Declarations

Competing interests

The authors declare no competing interests.

Additional information

Correspondence and requests for materials should be addressed to Z.H.

Reprints and permissions information is available at www.nature.com/reprints.

Publisher's note Springer Nature remains neutral with regard to jurisdictional claims in published maps and institutional affiliations.

Open Access This article is licensed under a Creative Commons Attribution-NonCommercial-NoDerivatives 4.0 International License, which permits any non-commercial use, sharing, distribution and reproduction in any medium or format, as long as you give appropriate credit to the original author(s) and the source, provide a link to the Creative Commons licence, and indicate if you modified the licensed material. You do not have permission under this licence to share adapted material derived from this article or parts of it. The images or other third party material in this article are included in the article's Creative Commons licence, unless indicated otherwise in a credit line to the material. If material is not included in the article's Creative Commons licence and your intended use is not permitted by statutory regulation or exceeds the permitted use, you will need to obtain permission directly from the copyright holder. To view a copy of this licence, visit <http://creativecommons.org/licenses/by-nc-nd/4.0/>.

© The Author(s) 2025